Proceedings of 20th International Congress on Acoustics, ICA 2010

23-27 August 2010, Sydney, Australia

Classical and non-classical nonlinear effects discerned by airborne ultrasound

Igor Solodov, Daniel Döring, and Gerd Busse

University of Stuttgart, Institute for Polymer Technology, Department of Nondestructive Testing, 70569 Stuttgart, Germany

PACS: 43.25.Dc; 43.25.Zx; 43.35.Zc; 43.38.Zp.

ABSTRACT

Nonlinear effects in air, which are regarded as fundamentals of classical nonlinear acoustics, were experimentally investigated mainly in a sonic frequency range. The present study extends the results into the ultrasonic frequency range of hundreds kHz. The acousto-optic technique of air-coupled vibrometry (ACV) has been adapted for imaging and non-invasive quantitative probing of nonlinear ultrasound in air. The technique was also applied to detection and visualization of high-frequency airborne ultrasound radiated by strongly nonlinear vibrations of cracked defects in solids (Nonlinear Air-Coupled Emission (NACE)). An efficient radiation of airborne higher harmonics enables to apply conventional air-coupled ultrasonic transducers for detecting NACE and use it as a nonlinear "tag" to locate and image the defects.

INTRODUCTION

Air-coupled vibrometry (ACV) is an acousto-optical method to visualize airborne sound fields [1]. It has been applied successfully in *linear* acoustics for imaging of leaky waves in plates [1] and calibration of air-coupled ultrasonic transducers [2]. The ACV enables non-invasive probing of airborne ultrasound and is far superior to the use of microphones which inevitably introduce a distortion in the acoustic field.

The microphone technique has nevertheless been a main measurement tool in nonlinear airborne acoustics. All experimental studies of acoustic nonlinearity in air known to us [3, 4] used a microphone receiver to detect and probe the higher harmonic and combination frequency fields. A similar approach served as a basis for classical measurements of the nonlinearity parameter of air [5].

In non-perfect solid materials, the acoustic nonlinearity develops due to strongly nonlinear vibrations in defect areas that makes it quite different from classical lattice nonlinearity. Such local nonlinear vibrations are accompanied by the radiation of high-frequency airborne ultrasound (Nonlinear Air-Coupled Emission (NACE) [6]) which is used as a nonlinear "tag" to detect and image the defects. Subject to adequate sensitivity, the ACV can serve as an approach to visualize the NACE and thus to find an application for defect-selective imaging in non-destructive testing.

In the present paper, the ACV is used for the measurements of the classical *nonlinear* effect of the second harmonic generation in air. The technique enables to visualize the second harmonic field to measure remotely and quantify its particle velocity along the propagation path. The non-classical nonlinear application includes a direct observation of NACE from damaged areas in solid materials and components.

NONLINEAR ULTRASONIC MEASUREMENTS IN AIR

Fundamentals of ACV

The ACV makes use of acousto-optic interaction between a narrow laser beam and airborne ultrasound caused by the photoelasticy of air: its refractive index (n) is a function of acoustic pressure (Δp):

$$\Delta n = (n_0 - 1)\Delta p / \rho_0 V^2 , \qquad (1)$$

where n_0 is the normal refractive index of air, ρ_0 is the undisturbed density, and V is the sound velocity in air.

As a result, the acoustic pressure induces a slight variation of the light velocity in air (c_{air}) which can be detected by a sensitive optical interferometric system. A periodic variation of acoustic pressure $\Delta p = p_0 \cos \omega t$ leads to the phase and frequency modulation of the light passed through an orthogonal acoustic beam (aperture L). Since for a plane acoustic wave in air $p_0 = v_p^0 \rho_0 V$ (v_p^0 is the amplitude value of particle velocity), the instantaneous frequency of the light wave received by the interferometer after reflection from a fixed screen takes the form:

$$f_i = f_0 (1 + 2\frac{L(n_0 - 1)\omega}{c_{air} n_0 V} v_p^0 \sin \omega t) \ . \qquad (2)$$

According to (2), the received laser light is frequency modulated at the ultrasonic frequency and the maximum frequency shift (modulation index) is proportional to the amplitude of

particle velocity. Subsequent mixing and frequency demodulation of the signal (2) enables to reproduce and measure the velocity waveform.

A similar task is routinely implemented in a standard Polytec vibrometer which measures the frequency modulation induced by vibrations of the reflector surface (amplitude of vibration velocity v_{ref}). In this case, the modulation index is the Doppler frequency shift:

$$\Delta f = \pm 2 f_0 v_{ref} / c_{air} \tag{3}$$

and the vibrometer is calibrated to read-out the values of v_{ref}.

By comparing (2) and (3), in the ACV experiment the vibrometer read-out should be changed to:

$$v_p^0 = \frac{n_0}{(n_0 - 1)KL} v_{ref} \quad , \tag{4}$$

where $K = \omega / V$ is the acoustic wave number.

In the near-field of a standard air-coupled ultrasonic transducer $L \sim 5\lambda$ and $KL \sim 30$, so that the correction factor in (4) is ~100. Since a reliable detection of the Doppler vibrometer starts from $v_{ref} \approx 10 \mu m/s$, the ACV sensitivity is estimated as $\approx 1 mm/s$. In the ACV experiment, relation (4) can be applied for evaluation of the absolute values of particle velocities in acoustic waves (v_p^0) on the basis of standard vibrometer readings (v_{ref}).

ACV of the second harmonic in air

When a plane acoustic wave is traveling in a nonlinear medium, each point of its waveform moves with a different phase velocity [5]:

$$V = V_o + \beta v_p \,, \tag{5}$$

which depends on the particle velocity v_p in that point. The factor β (nonlinearity parameter) includes the two nonlinear sources: the adiabatic equation of state and the continuity of a deformed medium.

For air, $\beta = (\gamma + 1)/2 = 1.2$ [5], where γ is the ratio of specific heat capacities. As the wave propagates, its waveform acquires a growing distortion that can be described as the built-up of the higher harmonic components. The harmonic content is obtained by expanding the distorted waveform into a power series of the amplitude Mach number $M_0 = v_p^0 / V$.

In a weakly nonlinear regime ($M_0 << 1$, $v_p^0 = \text{const}$), the major nonlinear contribution comes from the second harmonic whose amplitude in the lack of dissipation grows linearly with propagation distance x. In a dissipative medium (characterized by the attenuation factor α_0 for a small amplitude fundamental frequency ω wave), this growth is counteracted by an exponential decay of both the plane fundamental wave and its second harmonic:

$$v(x,t) = v_p^0 e^{-\alpha_o x} \sin(\omega t - Kx) + \frac{\beta \omega M_0^2}{4\alpha_o} \left[e^{-2\alpha_o x} - e^{-4\alpha_o x} \right] \sin[2(\omega t - Kx)] \tag{6}$$

In the experiment (Fig. 1), the ACV was used to visualize and measure the nonlinear airborne field (6) generated by a 200 kHz air-coupled transducer. To produce an intense acoustic wave in air, the input voltage of up to 120 V p/p CW was applied to the transducer. The laser beam reflected from a fixed screen (Fig. 1) was processed in the controller unit of the Polytec 300 vibrometer. After a 2D-scan and FFT of the received signal, the C-scan images of the wave propagation are obtained for the fundamental frequency and its second harmonic (Figs. 2, 3).

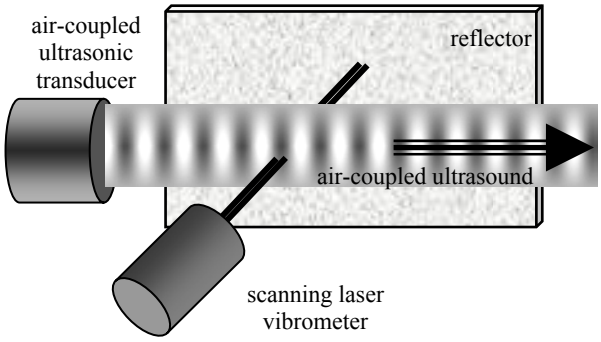

Fig. 1. Experimental set-up for ACV.

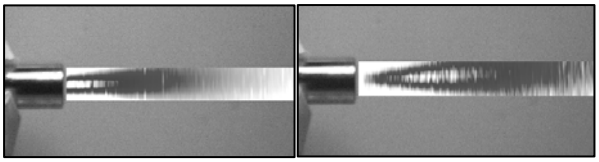

Fig. 2. Images of fundamental frequency (200 kHz) air-coupled beam (left) and its second harmonic (400 kHz, right).

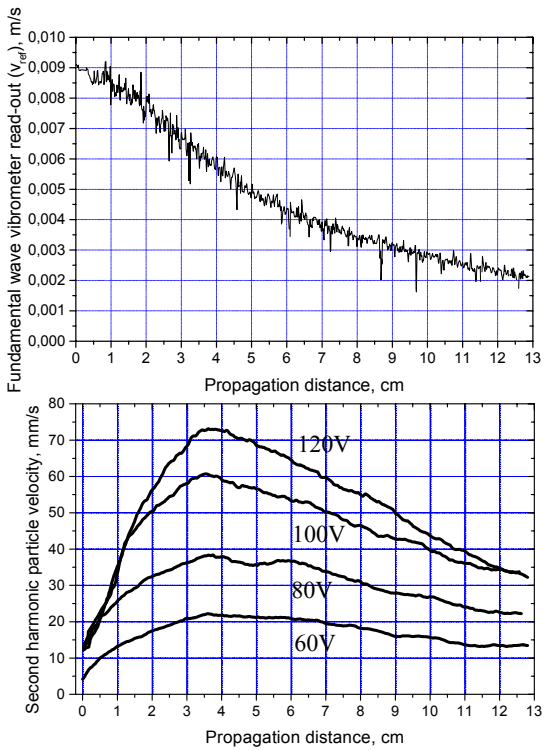

Fig. 3. Plot profiles for fundamental wave (top) and its second harmonic for various input voltages (bottom).

The second harmonic amplitude profile plots (Fig. 3, bottom) indicate a typical nonlinear behaviour: a quasi-linear growth

with distance followed by the amplitude decrease due to dissipation. The balance between these processes is reached at the so-called stabilization distance where the second harmonic is maximal. From (6), this value depends on the wave attenuation, so that $x_{stab} = \ln 2 / 2\alpha_0$; the data in Fig. 3 show that $x_{stab} \approx 35mm$ in our experiment. To quantify the fundamental wave attenuation, the profile plots similar to that in Fig. 3, top were obtained for different input voltages and interpolated with the exponential functions $\sim \exp(-\alpha x)$. The small amplitude value $\alpha_0 \approx 0.095cm^{-1}$ for 20V input yields from (6): $x_{stab} \approx 37mm$ that agrees well with the experimental result.

Fig. 4 illustrates the quadratic dynamic behaviour of the second harmonic stipulated by (6). The maxima of the second harmonic amplitudes at $x = x_{stab}$ in Fig. 3 (bottom) are plotted as functions of the input voltage. A distinct agreement with quadratic approximation is readily seen.

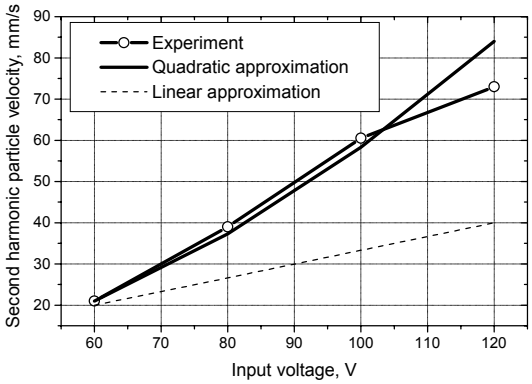

Fig. 4. Second harmonic amplitude as a function of input voltage.

Besides the capability of visualization of nonlinear fields, an important merit of the ACV is concerned with an opportunity for comprehensive quantification of the nonlinear effects. It requires the measurements of the absolute values of the particle velocity (displacement) amplitudes for the fundamental wave and the higher harmonics (see (6)), which has always been a challenge for classical nonlinear acoustics. As it was mentioned above, the ACV-measurements of the wave amplitudes are possible on the basis of relation (4).

For the 200 kHz transducer used, $KL \approx 33$ (at the fundamental frequency) so that from (4): $v_p^0 \approx 100 v_{ref}$. The application of this relation to the vibrometer data in Fig. 3 (top) yields the amplitude of the particle velocity in the fundamental wave (at $x = 0$) $v_p^0 \approx 90cm/s$ and the Mach number $M_0 \approx 2.6 \cdot 10^{-3}$. An analogous procedure was used to convert the second harmonic vibrometer data into the absolute velocity values presented in Fig. 3.

To verify the particle velocity value obtained with ACV, similar measurements were implemented by using the air-coupled radiometry. The radiation force the wave exerted on a $9x9\,mm$ aluminium foil pendulum reflector was measured to be $\approx 32\mu N$ resulting in the radiation pressure $P_{rad} \approx 0.4Pa$. The particle velocity is then derived as follows: $v_p^0 = \sqrt{2P_{rad} / \rho_0} \approx 84cm/s$ that confirms the validity of the ACV measurements.

These measurements therefore provide a complete set of experimental data to quantify the second harmonic generation in air on the basis of Eq. (6): $v_p^0 \approx 90cm/s$; $M_0 \approx 2.6 \cdot 10^{-3}$; $\alpha_0 \approx 0.095cm^{-1}$; $\omega = 2\pi \cdot 2 \cdot 10^5$, and $\beta = 1.2$ [5]. The results of calculations of the second harmonic field along the propagation distance from (6) are presented in Fig. 5 and demonstrate a close compliance with the experimental data.

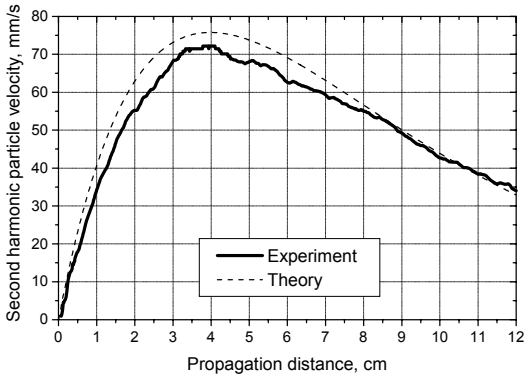

Fig. 5. Second harmonic amplitude as a function of distance.

The nonlinear waveform distortion is determined by the ratio of the second harmonic to the fundamental wave amplitude. This parameter can be readily evaluated from the ACV measurements of both the acoustic fields as functions of the propagation distance (Fig. 3). The expected behaviour can also be derived as the ratio of the two terms in Eq. (6) using the above set of experimental data. Such a comparison is given in Fig. 6. Due to dissipation of the fundamental wave the maximum waveform distortion is shifted from x_{stab} to $x_{\max} = \ln 3 / 2\alpha_0 \approx 60mm$. At this distance the second harmonic amplitude is close to 15% of the fundamental wave that results in some additional (nonlinear) attenuation which was also observed experimentally.

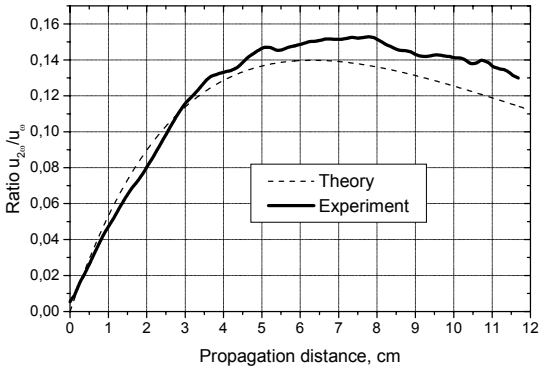

Fig. 6. Ratio between second harmonic and fundamental wave amplitudes as a function of propagation distance.

MEASUREMENTS OF NON-CLASSICAL NONLINEARITY OF DEFECTS

It is known that planar material defects (cracks, delaminations, non-bonded lap-joints, etc.) have strong nonlinear elastic properties and generate multiple nonlinear spectral components when driven by a sinusoidal acoustic wave. These nonlinear vibrations of defects are accompanied by the generation of acoustic waves in ambient air (NACE) that has recently been proposed for detection and imaging of defects

[6]. The ACV measurements can be used to visualize and quantify the NACE radiation patterns.

To produce intense acoustic vibrations that are required for the nonlinear regime, an ultrasound welding piezoelectric stack transducer was driven with a 40 kHz-CW electric signal to excite flexural waves. For maximum input voltage, the elastic strain produced in the specimens was in the range of ($10^{-5}-10^{-4}$). The focused beam of a laser vibrometer was aligned parallel to the specimen surface and scanned the air area above it (Fig. 7). After the scan and FFT of the signal received, the C-scan images of airborne fields are obtained for any spectral line within the frequency bandwidth of 1 MHz.

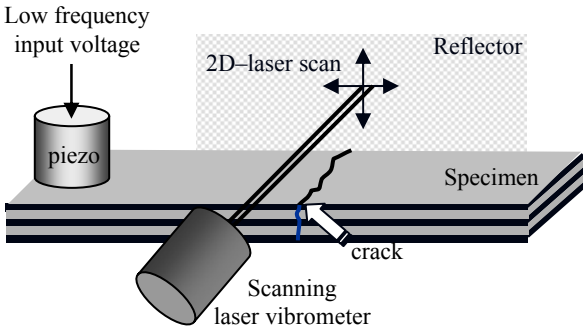

Fig. 7. Experimental set-up for ACV measurements of NACE.

Figure 8 shows the ACV images of airborne acoustic fields at the fundamental frequency and its second harmonic radiated by a cracked rod (*8x25x350 mm*) of carbon fiber-reinforced plastic (CFRP). The fundamental frequency field (Fig. 8, left) illustrates a classical propagation of a leaky flexural wave in the rod accompanied by a phase matched plane wave in air (with ACV measured velocity amplitude $v_{ref} \approx 470\mu m/s$) perturbed slightly by the presence of the defect. The second harmonic emission pattern (Fig. 8, right) reveals the two important features: firstly, it shows no radiation from outside the defect and thus confirms the concept of a defect as a localized source of nonlinear emission. Secondly, the NACE directivity pattern consists of a few side-lobes (with maximum vibrometer velocity read-out $v_{ref} \approx 130\mu m/s$) and is therefore quite distinct from a cylindrical (or spherical) wave one would expect from a line (or point) source.

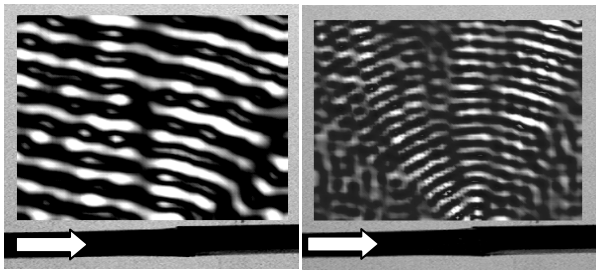

Fig. 8. Airborne fields over a cracked CFRP specimen: left - fundamental frequency (flexural wave propagates from left to right); right – second harmonic pattern.

To quantify the NACE, equation (4) is applied to convert the measured ACV data into realistic values of the particle velocities in air. For $L \approx 25mm$ at 40 kHz, the correction factor in (4) is ≈ 180, so that the amplitude of particle velocity in the fundamental frequency leaky wave in air is: $(v_p^0)_\omega \approx 85mm/s$. To verify this estimate, a standard laser vibrometry measurement (laser scanning of the specimen surface) was carried out which yielded the value of amplitude particle velocity (normal component) in the CFRP specimen as high as $\approx 80mm/s$. Taking into account the leaky wave radiation angle ($\approx (20-30^0)$), the ACV estimate agrees well with the boundary condition of continuity of the normal particle velocity component.

A similar procedure applied to the second harmonic field gives $KL \approx 90$ and thus $(v_p^0)_{2\omega} \approx 12mm/s$, i.e. about *14%* of the fundamental frequency vibrations are converted into the second harmonic in the crack area. This value might be even higher in reality because the wave front of the radiated second harmonic is unlikely parallel to the laser beam over the total interaction length. According to [1], that reduces the KL value in (4) and therefore increases $(v_p^0)_{2\omega}$. Whatever the case, the second harmonic signal is far above (3 orders of magnitude) the sensitivity of air-coupled transducers ($\sim 10\mu m/s$), which were first applied for the NACE detection in [6]. The high amplitude of the second harmonic is also confirmed by a strong nonlinear distortion of the local crack vibrations shown in Fig. 9.

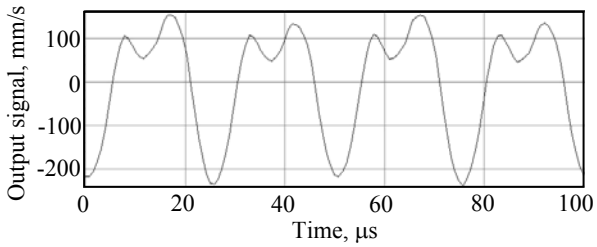

Fig. 9. Waveform distortion in the cracked area of CFRP rod.

The ACV enables not only to quantify the radiation efficiency of the nonlinear source (defect) but also to characterize the defect by identifying its NACE pattern. In fact, an omnidirectional radiation is expected from the defects whose size D is smaller than the wavelength in air: $KD << 1$. For larger defects, the radiation has an evident directivity in the far field. A few higher harmonic radiation patterns for such a defect ($25mm$ -long delamination) on the surface of a piezo-actuator embedded in *1.5x35x350mm* glass fibre-reinforced plastic (GFRP) plate are shown in Figs. 10. The piezo-actuator itself was used for excitation of oppositely directed 50kHz elastic waves in the specimen. The higher harmonic NACE fields observed with the ACV feature a distinct directivity dominated by the two symmetrically slanted side-lobes (Fig. 10).

The directivity of the radiated field is known to be a spatial Fourier transform of the vibration velocity distribution in the source area [7]. We assume the defect area as a continuous distribution of the nonlinear (n -th order higher harmonic) velocity sources over the length D:

$$w_n(x) = w_0 \Pi(x/D)\exp(jn\omega t), \qquad (7)$$

where the rectangle function $\Pi(x/D) = 1$ for $|x| < D/2$ and zero otherwise.

The higher harmonic vibrations (7) are activated by the oppositely propagating fundamental waves in the specimen which introduce progressive time delay $\pm x/c$ in subsequent

excitation of the higher harmonic sources so that $t \to t \pm x/c$ in (7). After this change, the Fourier transform of (7) is found as follows:

$$W_n(\theta) = w_0 D\, sinc[(nKD/2)(\sin\theta \pm \sin\theta_0)], \quad (8)$$

where $\sin\theta_0 = c_{air}/c$.

There are two evident conclusions inferred from the equation obtained:
- Directivity pattern (8) features two main side-lobes steered to $\pm\theta_0$ from the specimen normal. The beam steering angle is determined by the well-known Cherenkov`s radiation condition.
- The angular width of the side-lobes (determined by nKD factor) reduces for the higher-order harmonic NACE.

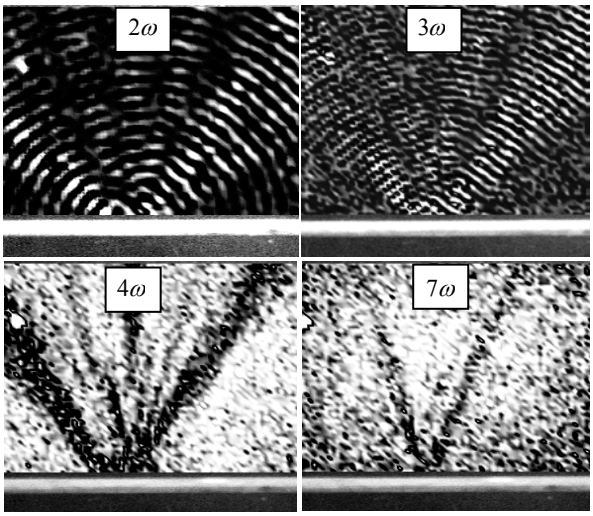

Fig. 10. NACE fields of various higher harmonics from delamination in GFRP

Both conclusions are supported by the ACV images shown in Fig. 10. The two symmetrical main side-lobes are clearly observed for all higher harmonics. The second harmonic NACE field exhibits maximum angular width of the side-lobes. The images in Fig. 10 also demonstrate that the radiation angle θ_0 reduces as the harmonic number increases: from $\approx 45^0$ for the second harmonic to $\approx 20^0$ for the seventh harmonic. This corresponds to an about twofold increase in velocity c (from about $500 m/s$ to $1000 m/s$) in the frequency range $(100-350)\ kHz$. Such a variation is in a good agreement with the $\sqrt{\omega}$ dispersion law for the flexural waves in thin plates. The opportunity to apply the radiation condition to locate the major part of the NACE field makes a reasonable approach to positioning of air-coupled detectors in the NACE imaging configuration [6].

For small angles of radiation and extended defect area, the symmetrical beams overlap and interfere to form the wave propagating along the normal to the specimen (the z-axis):

$$v(x,z) = 2v_0 \cos K_x x \cos(\omega t - K_z z). \quad (9)$$

The ACV image of such a NACE field observed for an extended delamination in a large fiber-reinforced concrete plate ($450x100x11 mm$) is given in Fig. 11. The pattern is measured for a 40 kHz drive at 62 kHz NACE component originated from a frequency pair doublet [8] of 18 kHz and 22 kHz. The standing wave distribution along the x-axis in (9) provides the system of vertical nodal lines in the airborne field. The anti-phase wave propagation along the z-axis in the adjacent channels stipulated by (9) is also clearly seen.

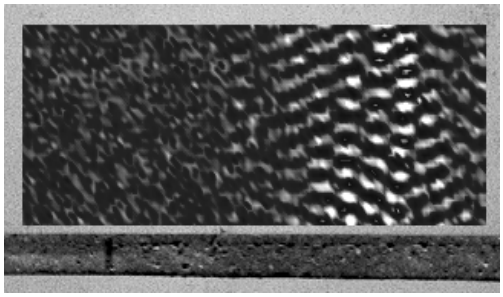

Fig. 11. NACE from an extended delamination area in a concrete plate.

The pattern in Fig. 11 indicates the formation of the standing wave in the delamination area and thus supports the approach based on the contra-flowing wave excitation of the defect area used above to interpret the NACE wave fields.

NACE FOR DEFECT-SELECTIVE IMAGING AND NDE OF DEFECTS

A practical version of the NACE for nonlinear imaging of defects uses a high-frequency focused air-coupled ultrasonic transducer as a receiver to match the radiation directivity pattern by variation of its reception angle θ (Fig. 12). The transducer high-frequency band-pass response combined with high-pass filtering circuit provides a strong rejection of the excitation frequency signal. The nonlinear frequency components are then used as an input to commercial air-coupled scanning equipment (AirTech 4000) for computer imaging of the NACE amplitude distribution over a specimen surface (C-scan).

In the experiments, the piezo-stack transducer and high-power supply (Branson Ultrasonics) provided an intense low-frequency excitation with $\geq 10^{-6}$ strain amplitude in the source. A pair of focused (focus spot ~2-3 mm, focus distance 40 mm) AC-transducers with frequency responses centred at ~400 kHz and ~450 kHz (3 dB-bandwidth of ~20 kHz) were alternately used as receivers in the C-scan mode. The two excitation frequencies around 40 and 20 kHz were used to maximize the NACE signals around (9-11th) and (23-24th) higher harmonics, respectively.

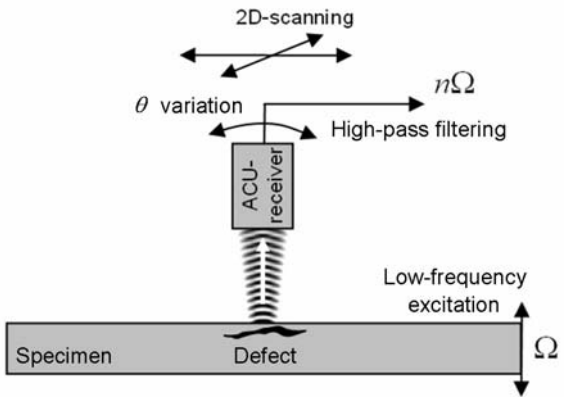

Fig. 12. Experimental set-up for NACE imaging and NDE of defects.

Unlike nonlinear laser scanning vibrometry (NSLV) [9], which analyzes the light *reflected* from the specimen, the NACE-imaging relies on direct nonlinear acoustic *radiation*

by the defects. For the weakly-focused AC-transducers with cm-range depth of focus, the receiver is insensitive to medium scale variations of the surface profile. This makes NACE in many cases a superior alternative methodology to locate and visualize the defects. A few examples of the NACE imaging and NDE of defects are given below.

In Fig. 13, the NACE imaging results are compared with NSLV of multiple impact damage on a reverse side of a carbon fibre-reinforced (CFR-) multi-ply ($+45^0$; -45^0) composite plate (*175x100x1 mm*). Both techniques reliably visualize the defects with similar sensitivity.

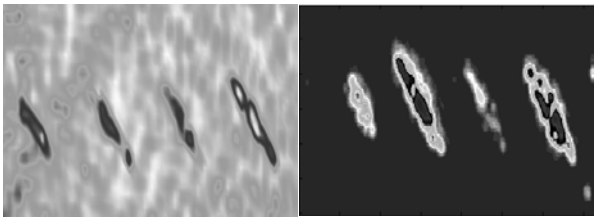

Fig. 12. NSLV (left) and NACE (right) imaging of impact induced damage in multi-ply ($+45^0$; -45^0) CFRP-plate.

Fig. 13 (left) shows the (9-11th) harmonic NACE image of the 50μm-wide fatigue crack in a steel plate (*150x75x5 mm*) with two horizontally located grip holes for cyclic loading at some distance from the crack. The image reveals that the NACE detects not only the crack itself but also the fatigue structural damage in the plasticity areas between the crack and the grip holes.

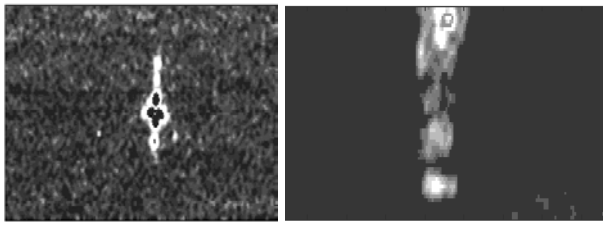

Fig. 13. NACE imaging in steel specimens (40 kHz-excitation): (9-11th) harmonic imaging of 50 μm-wide fatigue crack (left); hammer peening area in steel plate (right).

To verify the NACE sensitivity to micro-damage induced by plastic deformation, the NACE inspection was implemented for a steel specimen with a cold work area (*5x40 mm*) produced by hammer peening. The image in Fig. 13, right confirms that the NACE develops even without serious cracked defects and clearly discerns the micro-damage induced by plastic deformation.

CONCLUSIONS

The variation of local pressure in an airborne ultrasonic wave is high enough to induce the optical path modulation for the laser light passing through the acoustic beam. The ACV sensitivity (~1% of that for conventional laser vibrometry) enables to visualize nonlinear airborne fields in the frequency range of a few hundred kHz. The method is also capable of non-intrusive measuring of the absolute values of acoustic wave dynamic parameters (particle velocity, pressure) which has always been a challenge for classical nonlinear acoustics. A sufficient accuracy of the ACV nonlinear measurements is confirmed by a comprehensive quantitative fit of the experimental data with the classical relations for the build-up and decay of the second harmonic in air.

The ACV methodology is also applicable to imaging and quantification of the nonlinear airborne radiation produced by non-classical nonlinearity of planar defects. The high radiation efficiency measured for the airborne higher harmonics provides an ample "margin of safety" in detecting the NACE with conventional air-coupled transducers. The ACV imaging is also effective in defect characterization by identifying their far-field NACE patterns since the directivity of the radiated field is the spatial Fourier transform of the vibration velocity distribution in the source (defect) area.

Unlike conventional acoustic emission, which relies on detection of transient acoustic waves in the interior of materials, the NACE makes use of airborne ultrasound produced by nonlinear defects. The air-coupled methodology of "nonlinear listening" simplifies considerably location of the emission source and enables high-resolution imaging of damaged areas.

ACKNOWLEDGEMENT

The authors are grateful to the German Research Foundation for supporting this work as part of the project Bu 624/33-1 ("Akustische Nichtlinearität als selektiver Defektindikator in der zerstörungsfreien Prüfung").

REFERENCES

1 I. Solodov, D. Döring, and G. Busse, "Air-coupled laser vibrometry: analysis and applications" *Applied Optics*, **48**, 33-37 (2009)

2 L. Zipser and H. Franke, "Laser-scanning vibrometry for ultrasonic transducer development" *Sensors and Actuators*, **A110,** 264-268 (2004)

3 Tomoo Kamakura, Naoaki Hamada, Kenich Aoki, and Yoshiro Kumamoto, "Nonlinearly generated spectral components in the nearfield of a directive sound source" *J. Acoust. Soc. Am*., **85**, 2331-2337 (1989)

4 Tomoo Kamakura, Meiko Tani, and Yoshiro Kumamoto, "Harmonic generation in finite amplitude sound beams from a rectangular aperture source", *J. Acoust. Soc. Am*., **91**, 3144-3151 (1992)

5 Robert Beyer, *Nonlinear Acoustics*, Published by the Acoustical Society of America, 1997.

6 I. Solodov and G. Busse, "Nonlinear air-coupled emission: the signature to reveal and image micro-damage in solid materials", *Appl. Phys. Letts*., **91**, 251910 (2007)

7 E.G. Williams, *Fourier Acoustics: Sound radiation and nearfield acoustical holography*, Academic Press, New York, 1999

8 I. Solodov, J. Wackerl, K. Pfleiderer, and G. Busse, "Nonlinear self-modulation and subharmonic acoustic spectroscopy for damage detection and location", *Appl. Phys. Lett.*, **84**, 5386-5388 (2004)

9 I. Solodov, K. Pfleiderer, and G. Busse,"Nonlinear acoustic NDE: inherent potential of complete non-classical spectra" In: *Universality of Non-Classical Nonlinearity with Application to NDE and Ultrasonics,* Ed. P. Delsanto, (Springer Verlag, New York, USA, (2006) Ch. 29, pp. 465-484.